A Double-Sided *LCL*-Compensated Network for the Strongly Coupled CPT System With Minimum Plate Voltage Stresses

Ting Chen, *Member, IEEE*, Chenwen Cheng, Xian Zhang, Guangyao Li, Yanjie Guo, *Member, IEEE*, and Chunting Chris Mi, *Fellow, IEEE*

Abstract— In the conventional design of a double-sided *LCL* compensation network for the capacitive power transfer (CPT) system, two external capacitors are connected in parallel with the horizontal capacitive coupler, or a vertical capacitive coupler is required to reduce the resonant inductances. This approach results in a loosely coupled structure. The compensation inductor resonates with the whole coupler, inducing reactive power transferred from the primary to the secondary side, leading to higher voltage stresses on the plates, which inevitably increases the system complexity and susceptibility to air breakdown. This article proposes a double-sided *LCL* compensation network design method for the CPT system where no parallel-connected capacitors are required, thereby a strongly coupled structure can be obtained with a constant current (CC) output and input zero phase angle (ZPA) characteristics. By keeping the phase angle difference between the voltage vectors across the primary and secondary plates at 90°, no reactive power is transmitted from the primary to the secondary side. Thus, the voltage stresses across the plates can be minimized. A 500 W prototype with a high coupling coefficient of 0.82 is established to verify the proposed system and an efficiency of 90% is achieved.

Index Terms— Capacitive coupler, capacitive power transfer (CPT), *LCL* compensation topology, minimum voltage stresses, wireless power transfer (WPT).

I. INTRODUCTION

WIRELESS power transfer (WPT) is emerging as an alternative charging technology in various applications

Ting Chen, Xian Zhang, Guangyao Li, and Yanjie Guo are with the State Key Laboratory of Reliability and Intelligence of Electrical Equipment and Hebei Key Laboratory of Equipment and Technology Demonstration of Flexible DC Transmission, Hebei University of Technology, Tianjin 300401, China (e-mail: tingchen@hebut.edu.cn; zhangxian@hebut.edu.cn; lgymecury@163.com; yjguo@hebut.edu.cn).

Chenwen Cheng is with the School of Electrical Engineering, Southeast University, Nanjing 210096, China (e-mail: cheng.cwen@gmail.com).

Chunting Chris Mi is with the Department of Electrical and Computer Engineering, San Diego State University, San Diego, CA 92182 USA (e-mail: mi@ieee.org).

such as electrical vehicles [1], [2], [3], [4], [5], consumer electronics [6], unmanned aerial vehicles [7], [8], [9], automated guided vehicles [10], and autonomous underwater vehicles [11], [12]. According to the transmission mediums, WPT can be mainly classified as inductive power transfer (IPT) and capacitive power transfer (CPT) [13]. In IPT, the energy is transferred by the magnetic field [14]. When metal appears in the magnetic field, the eddy current loss in the metal will cause temperatures to rise, resulting in safety hazards [15], [16]. The CPT system can be presented as a substitute because it transfers energy through the electric field without eddy current issues, which makes CPT technology much safer when metal objects are surrounding. Besides, the CPT system exhibits lower cost and weight because it is made up of copper plates or aluminum plates rather than the Litz wires in the IPT system, which has had a recent wide scope of research [17], [18].

Like in IPT, compensation circuits such as *LCLC–LCLC* [19], *LC–LC* [20], *LCL–LCL* [21], *LCL-L* [22], and *CL-CL* [23] are essential to improve the CPT system's performance. The coupler structure in the CPT system is classified as the horizontal structure and the vertical structure as shown in Fig. 1. The equivalent circuit model and the simplified equivalent Π model of the coupling capacitors are shown in Fig. 2 [21], [24]. C_{ij} (i, j = 1, 2, 3, 4; $i \neq j$) is the coupling capacitor between P_i and P_j. C_M and C_1 (C_2) are the mutual capacitance and the self-capacitance, respectively. The coupling coefficient k_c can be derived as $k_c = C_M/C_1 = (C_{13} - C_{14})/(2C_{12} + C_{13} + C_{14})$ because of the symmetrical coupler structure. C_{13} (C_{24}) is much larger than C_{12} (C_{34}) and C_{14} (C_{23}) because the facing area is much larger, thereby the coupling coefficient in a CPT system is essentially high. In [19], a double-sided *LCLC*-compensated topology with a horizontal coupler structure was proposed. Usually, the self-capacitance in the horizontal coupler structure is only several tens of picofarads. Therefore, two additional capacitors have to be connected in parallel with the coupler to reduce the compensation inductance. However, external capacitors will increase system complexity. To reduce the total number of compensation components, Lu et al. [20] proposed a double-sided *LC*-compensation circuit topology with a horizontal coupler structure, which includes two external capacitors in parallel with the coupler and two compensation inductors. However, the control degree of freedom is limited
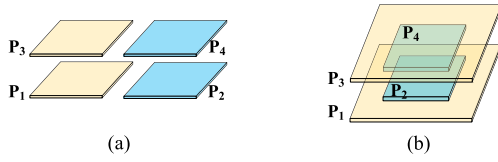
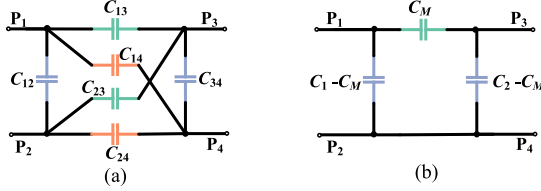Fig. 1. Capacitive coupler. (a) Horizontal structure. (b) Vertical structure.

Fig. 2. Equivalent circuit model of the capacitive coupler. (a) Circuit model of the coupling capacitors. (b) Simplified equivalent Π model of coupling capacitors.

because the output power of the system is only related to the coupling coefficient, the switching frequency, and the mutual capacitance. Zhang et al. [21] and Vu et al. [22] proposed a double-sided LCL-compensated topology and an LCL–L compensation topology, respectively with a vertical coupler structure. Two plates are placed vertically and close-set on the primary and secondary sides, respectively to increase the self-capacitances of the coupler so that no external capacitors are required. However, since the two plates on the primary and secondary sides are very close in vertical structure, the air between them may be prone to breakdown due to the high electric field. In the above CPT systems, the equivalent coupling exhibits a low coupling coefficient k_c because the external capacitors in the horizontal capacitive coupler or the large self-capacitors in the vertical capacitive coupler make C_{13} (C_{24}) increase, which leads to a loosely coupled capacitive coupler. Thus, the coupling coefficient in a CPT system is related to not only plate clearance but also the external parallel-connected capacitances. It should be noted that this characteristic is different from the IPT system where the low coupling coefficient is because of the long distance between couplers [16].

In the design method shown above, the compensation inductor resonates with the whole coupler rather than the self-capacitor, inducing a nonresistive secondary impedance. Thus, reactive power is transferred from the primary side to the secondary side, which leads to higher voltage stresses on the plates. In this case, a strong electric field emission appears, and the possibility of dielectric breakdown increases. Moreover, the compensation capacitor's voltage rating must be increased, which also increases costs. Thus, Mai et al. [23] proposed a component voltage stress optimization method for the double-sided CL-compensated system by reallocating the voltage stress on the circuit components. Although no external capacitors are in parallel with the coupler, the component voltage optimization design procedure relies on the initial value, and complicated mathematical calculations are needed. Lian and Qu [25] and Lian et al. [26] proposed the parameter design method under the premise of specific coupler voltage ratings for the double-sided LC-compensated system

and the double-sided $LCLC$-compensated system, respectively. However, the phase angle difference between the primary-side and the secondary-side plate voltages is not 90°, so the voltage across the coupler is still not at the minimum value.

In this article, a double-sided LCL compensation network design method for the strongly coupled horizontal capacitive coupler is proposed. The derived compensation network structure aligns with that presented in [19] and [21], which are considered the benchmark for comparison with the proposed approach. It is noteworthy that [19] and [21] share the same compensation network design method but employ different capacitive couplers. Hence, this article collectively refers to them as the conventional double-sided LCL compensation network design method. The contributions of this article are summarized as follows.

1) The proposed design method eliminates two additional external capacitors in parallel with the coupler, the compensation circuit is simplified, and the risk of air breakdown is mitigated.
2) Reactive power transferred between the primary and secondary sides is eliminated with the proposed compensation network design method. Consequently, the plate voltage stress can also be minimized.
3) In a strongly coupled scenario, the proposed design methodology yields significantly smaller compensation inductances, thereby the system volume is reduced. Thus, the proposed compensation method is more suitable for a strongly coupled CPT system.

The remainder of this article is as follows. Section II elaborates on the weakness of the conventional design method for the double-sided LCL-compensated CPT system. Section III proposes a design method for the double-sided LCL-compensated CPT system and gives an analysis of voltage stresses and system efficiency. Experiment and simulation results are provided in Section IV to validate the presented system design method.

II. ANALYSIS OF REACTIVE POWER GENERATION

A. System Description and Reactive Power Analysis

Fig. 3(a) shows the circuit structure of the double-sided LCL-compensated CPT system. V_{dc} is the dc source. S_1, S_2, S_3, and S_4 are four metal oxide semiconductor field effect transistors (MOSFETs), which form the high-frequency inverter. V_{ab} is the inverter output voltage. L_{f1}, C_{f1}, and L_1 form the primary LCL resonate circuit. L_{f2}, C_{f2}, and L_2 form the secondary LCL resonant circuit. A full-bridge rectifier formed by four diodes D_1, D_2, D_3, and D_4, and a filter capacitor C_l is adopted before a real load R_o at the receiving side to transform the ac power to a dc source. It is noteworthy that there is no requirement for external capacitors to be paralleled with the horizontal coupler. To simplify the following analysis, the full-bridge rectifier with a real load is regarded as resistive and can be modeled as a load resistance R_L [27], and the equivalent behavior-source model is shown in Fig. 3(b). It should be noted that C_1 and C_2 only represent the internal self-capacitances when the proposed design method is
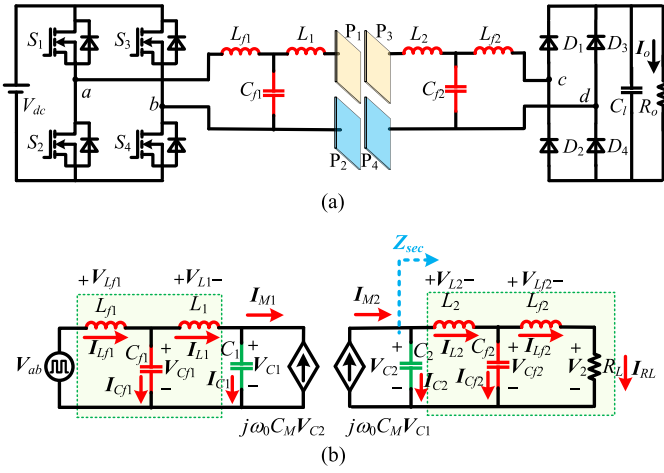
(a)

(b)

Fig. 3. Double-sided *LCL*-compensated CPT system with a strongly coupled horizontal capacitive coupler. (a) Circuit structure. (b) Equivalent behavior-source model.

Fig. 4. Reactive power analysis with the conventional double-sided *LCL* compensation network design method. (a) Phase angle difference versus coupling coefficient. (b) Product of V_{C1} and V_{C2} versus the reactive power with different coupling coefficients.

employed. The induced current sources I_{M1} and I_{M2} can be expressed as

$$I_{M1} = -j\omega_0 C_M V_{C2}, \quad I_{M2} = j\omega_0 C_M V_{C1} \tag{1}$$

where ω_0 is the resonant angular frequency and $\omega_0 = 2\pi f_0$. f_0 is the resonant frequency. V_{C1} and V_{C2} are the voltage vectors across the primary plates and the secondary plates, respectively.

The apparent power S transferred from the primary side to the secondary side is a combination of active power P and reactive power Q, which can be expressed as

$$S = P + jQ = V_{C1} \cdot (-j\omega_0 C_M V_{C2})^* \tag{2}$$

where "$*$" is the conjugate of the corresponding variable. It is noteworthy that the reactive power is zero and the transferred active power reaches the maximum value only when the phase angle difference between V_{C1} and V_{C2} is 90°.

In order to discover the condition when the 90° phase angle difference between V_{C1} and V_{C2} can be achieved, the secondary side impedance Z_{sec} in the CPT system of Fig. 3 can be calculated as

$$Z_{\text{sec}} = V_{C2}/I_{M2} = V_{C2}/\left(j\frac{1}{Z_{\text{CM}}}V_{C1}\right). \tag{3}$$

It can be observed from (3) that when the secondary side impedance is resistive, the phase angle difference between V_{C1} and V_{C2} is 90°. In this case, no reactive power is transferred from the primary to the secondary side. The product of the primary-side and secondary-side plate voltages can be minimized given the specified active power demand.

B. Conventional Double-Sided LCL Compensation Network Design Method

The equivalent behavior-source model of the derived double-sided *LCL* compensation network employing the conventional design method for the CPT system is the same as in Fig. 3(b) [19], [21]. The resonance conditions derived from the proposed design method differ from those obtained through the conventional design method, in which the compensation
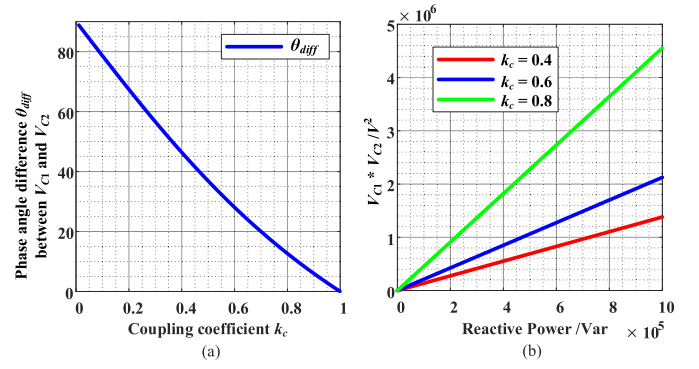
inductor resonates with the whole coupler. Furthermore, in the conventional design method, in order to reduce the compensation inductance, two external capacitors have to be connected in parallel to the horizontal capacitive coupler. A critical distinction to note is that C_1 and C_2 incorporate not only self-capacitance but also external capacitance. Alternatively, two plates need to be very close to form a vertical capacitive, thereby increasing the self-capacitances. The resonant conditions are expressed as [19], [21]

$$\begin{cases} \omega_0^2 = 1/(L_{f1}C_{f1}) = 1/(L_{f2}C_{f2}) \\ \omega_0^2 = \dfrac{1}{L_1 C_{f1}} + \dfrac{1}{L_1(1-k_c^2)C_1} = \dfrac{1}{L_2 C_{f2}} + \dfrac{1}{L_2(1-k_c^2)C_2}. \end{cases} \tag{4}$$

The phase angle difference θ_{diff} between V_{C1} and V_{C2} can be derived as [19], [21]

$$\theta_{\text{diff}} = \arctan\left(\frac{\omega_0 C_{f2}^2 \cdot V_2^2}{C_2(1-k_c^2)P_L}\right) - \arctan\left(\frac{\omega_0 C_{f2}^2 k_c^2 \cdot V_2^2}{C_2(1-k_c^2)P_L}\right) \tag{5}$$

where V_2 is the load voltage and P_L is the output power. The following analysis is taken from the experimental parameters as shown in Section IV, in which $V_{\text{dc}} = 90$ V, $P_L = 500$ W, $C_M = 37.86$ pF. According to Fig. 4(a), θ_{diff} decreases with the increasing coupling coefficient, which indicates that more reactive power is transferred with a higher coupling coefficient. According to Fig. 4(b), the product of V_{C1} and V_{C2} increases with the growing reactive power under the premise of fixed active power. Moreover, the product of V_{C1} and V_{C2} increases with increasing coupling coefficient. Thus, if the same amount of active power is required, V_{C1} or V_{C2} will increase when more reactive power flows between the primary and secondary sides. This is owing to the fact that the compensation inductor resonates with the whole capacitive coupler, leading to the nonresistive equivalent impedance in the secondary side as indicated in (3).

III. PROPOSED DOUBLE-SIDED LCL COMPENSATION NETWORK DESIGN METHOD

Due to the bandpass characteristic of the resonant CPT system, the fundamental harmonics approximation (FHA) method

can be used to analyze the circuit when higher-order harmonics are neglected [21]. Furthermore, all resonate components are assumed to be ideal with no parasitic resistances. In order to eliminate the reactive power transmission in the CPT system, it is imperative to ensure that the phase angle difference between V_{C1} and V_{C2} is 90°, which requires the redesign of the compensation circuits.

A. Derivation of the Compensation Topology

Usually, the L-section matching network [28], [29] or the gyrator model [30] can be used to design the WPT system. Compared to the gyrator model, the L-section matching network with only two components contributes to the simplification of the design process. Thus, this article adopts the L-section matching network to design the system. The schematic of the proposed double-sided *LCL*-compensated CPT system is shown in Fig. 5, which contains six blocks. Blocks 1, 3, and 5 are voltage-fed reversed L-section matching networks. Block 2 is the current-fed normal L-section matching network. The abovementioned four blocks comprise an inductor reactance and a capacitor reactance of equal value. Block 4 is a capacitor reactance. Block 6 is an inductor reactance. Z_1, Z_2, Z_3, Z_4, Z_5, and Z_6 represent resonant component reactance and are all positive. $(-jZ_3)$ and $(-jZ_4)$ are equivalent to self-capacitors C_1 and C_2, respectively. It should be noted that C_1 and C_2 are only the internal self-capacitances of the equivalent Π-model of the capacitive coupler and there are no external self-capacitances.

The L-section matching network driven by a voltage source or a current source can achieve constant current (CC) output or constant voltage (CV) output, respectively [28]. Thus, on the primary side, the fundamental component of inverter output voltage V_1 is converted to a CC output I_a through Block 1, then to a CV output V_a through Block 2, and finally to a CC output I_{M1} through Block 3. According to (1), V_{C2} is only relevant to I_{M1}, so V_{C2} is a CV and can be calculated as

$$V_{C2} = I_{M1} \cdot \frac{Z_{CM}}{-j} = \frac{V_a}{jZ_3} \cdot \frac{Z_{CM}}{-j} = \frac{I_a \cdot jZ_2}{jZ_3} \cdot \frac{Z_{CM}}{-j}$$
$$= \frac{V_1}{jZ_1} \cdot \frac{jZ_2}{jZ_3} \cdot \frac{Z_{CM}}{-}j = \frac{Z_{CM}Z_2}{Z_1Z_3}V_1 \qquad (6)$$

where $Z_{CM} = 1/(\omega_0 C_M)$. On the secondary side, V_{C2} is converted to a CC output I_{RL} through Block 5, which can be calculated as

$$I_{RL} = V_{C2}/jZ_5 = Z_{CM}Z_2 V_1/(jZ_1Z_3Z_5). \qquad (7)$$

In Fig. 5, after the coupler is determined with respect to the requirements in the specific application, Z_3 and Z_4 are known, which can be expressed as

$$Z_3 = 1/(\omega_0 C_1), \ Z_4 = 1/(\omega_0 C_2). \qquad (8)$$

The secondary side impedance Z_{sec} can be derived as

$$Z_{\text{sec}} = 1 \Big/ \left[\frac{R_L}{Z_5^2} + j\left(\frac{1}{Z_4} - \frac{1}{Z_5} + \frac{Z_6}{Z_5^2} \right) \right]. \qquad (9)$$

According to (3), Z_{sec} should be purely resistive to ensure that the phase angle difference between V_{C1} and V_{C2} is 90°,
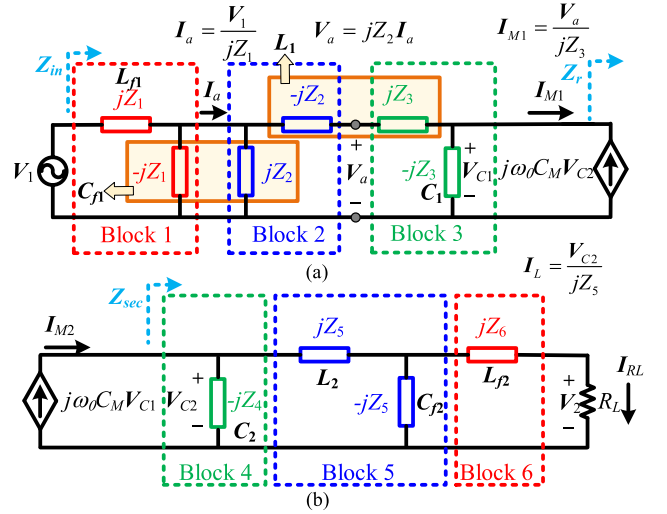

Fig. 5. Schematic of the proposed design method for the double-sided *LCL*-compensated CPT system. (a) Primary side. (b) Secondary side.

so the following condition should be met:

$$Z_6 = Z_5(Z_4 - Z_5)/Z_4. \qquad (10)$$

Considering Z_4, Z_5, and Z_6 in (10) are positive, the secondary compensation network is an *LCL*-compensated circuit as shown in Fig. 5(b), where jZ_5, $(-jZ_5)$, and jZ_6 are equivalent to an inductor L_2, a capacitor C_{f2}, and an inductor L_{f2}, respectively. Furthermore, since the impedance Z_4 of the self-capacitance in the horizontal coupler is usually large, it can be obtained that $Z_4 > Z_5$, which indicates a smaller L_2 of the secondary compensation circuit.

The secondary side impedance Z_{sec} seen from the primary side is defined as the reflected impedance Z_r, which can be derived as

$$Z_r = V_{C1}/I_{M1} = 1 \big/ \left[(\omega_0 C_M)^2 Z_{\text{sec}} \right]. \qquad (11)$$

The primary side impedance Z_{in} can be calculated as

$$Z_{\text{in}} = 1 \Big/ \left[\frac{Z_2^2 Z_r}{Z_1^2 Z_3^2} + j\left(\frac{Z_2}{Z_1^2} - \frac{1}{Z_1} - \frac{Z_2^2}{Z_1^2 Z_3} \right) \right]. \qquad (12)$$

Under the premise that the secondary side impedance is resistive, for the sake of realizing input zero phase angle (ZPA), the following equation should be met to obtain a resistive Z_{in}:

$$Z_1 = Z_2(Z_3 - Z_2)/Z_3. \qquad (13)$$

Considering Z_1, Z_2, and Z_3 in (13) are positive, it can be obtained that $Z_3 > Z_2 > Z_1$. jZ_1 is equivalent to an inductor L_{f1}. The parallel circuit of $(-jZ_1)$ and jZ_2 is equivalent to a capacitor C_{f1}. The series circuit of $(-jZ_2)$ and jZ_3 is equivalent to an inductor L_1. Thus, the primary compensation network is also an *LCL*-compensated circuit as shown in Fig. 5(a). Moreover, $Z_3 - Z_2$ is smaller than Z_3, so the equivalent inductance L_1 is not too large, which indicates a smaller inductor of the primary compensation circuit.

It can be obtained from (9)–(13) that the primary side impedance is inversely proportional to the load resistance,

which indicates that the removal of the pick-up does not result in the generation of excessive over-currents and over-voltages. Thus, the proposed system is beneficial to be used in applications where the secondary side moves in and moves out.

B. System Parameter Design

Since R_L is a purely resistive load, I_{RL} is in phase with the load voltage V_2, and the output power P_L can be derived as

$$P_L = I_{RL}V_2 = Z_{CM}Z_2V_1V_2/Z_1Z_3Z_5. \qquad (14)$$

According to the power balance, the following equation can be obtained:

$$V_2 \cdot I_{RL} = V_{C2} \cdot I_{M2}. \qquad (15)$$

Substituting (1) and (7)–(15), V_{C1} can be derived as

$$V_{C1} = Z_{CM}V_2/Z_5. \qquad (16)$$

When the output power P_L is specified, in order to minimize the voltages across the primary side and the secondary side at the same time, V_{C1} should be equivalent to V_{C2}. Thus, the following equation should be satisfied:

$$V_1/V_2 = Z_1Z_3/(Z_2Z_5). \qquad (17)$$

Therefore, under the premise that V_1, V_2, P_L, and the capacitive coupler are specified, substituting (17) into (14), Z_5 can be calculated as

$$Z_5 = \sqrt{Z_{CM}V_2^2/P_L}. \qquad (18)$$

Z_6 can be derived from (10) and (18), which can be expressed as

$$Z_6 = \sqrt{Z_{CM}V_2^2/P_L - Z_{CM}V_2^2/(Z_4P_L)}. \qquad (19)$$

According to (13), (17) and (18), Z_2 can be calculated as

$$Z_2 = Z_3 - \sqrt{Z_{CM}V_1^2/P_L}. \qquad (20)$$

Z_1 can be derived from (13) and (20), which is expressed as

$$Z_1 = \sqrt{Z_{CM}V_1^2/P_L - Z_{CM}V_1^2/(Z_3P_L)}. \qquad (21)$$

Based on (8), (18)–(21), Z_1–Z_6 are listed in Table I. The compensation inductances and capacitances are calculated as (22). In the case of $V_1 = V_2$ and $Z_3 = Z_4$, $L_{f1} = L_{f2}$, $C_{f1} = C_{f2}$, and $L_1 = L_2$ can be derived. The flowchart of the proposed parameter design for the double-sided

TABLE I
IMPEDANCES WITH THE PROPOSED METHOD

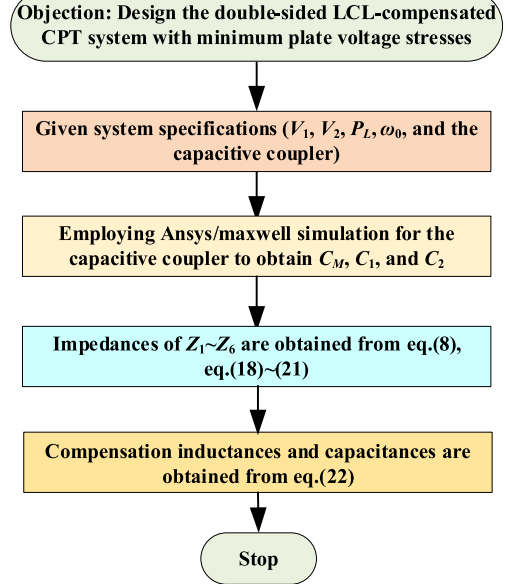| Z_1	Z_2	Z_3
$\sqrt{\dfrac{Z_{CM}V_1^2}{P_L} - \dfrac{Z_{CM}V_1^2}{Z_3P_L}}$	$Z_3 - \sqrt{\dfrac{Z_{CM}V_1^2}{P_L}}$	$\dfrac{1}{\omega_0 C_1}$
Z_6	Z_5	Z_4
$\sqrt{\dfrac{Z_{CM}V_2^2}{P_L} - \dfrac{Z_{CM}V_2^2}{Z_4P_L}}$	$\sqrt{\dfrac{Z_{CM}V_2^2}{P_L}}$	$\dfrac{1}{\omega_0 C_2}$

Fig. 6. Flowchart of the proposed parameters design for the double-sided *LCL*-compensated CPT system.

LCL-compensated CPT system is shown in Fig. 6

$$\begin{cases} L_{f1} = \dfrac{Z_1}{\omega_0} = \dfrac{1}{\omega_0}\left(\sqrt{\dfrac{Z_{CM}V_1^2}{P_L}} - \dfrac{Z_{CM}V_1^2}{Z_3P_L}\right) \\[2ex] L_{f2} = \dfrac{Z_6}{\omega_0} = \dfrac{1}{\omega_0}\left(\sqrt{\dfrac{Z_{CM}V_2^2}{P_L}} - \dfrac{Z_{CM}V_2^2}{Z_4P_L}\right) \\[2ex] C_{f1} = \dfrac{(Z_2 - Z_1)}{Z_1Z_2\omega_0} = \dfrac{1}{\omega_0}\sqrt{\dfrac{P_L}{Z_{CM}V_1^2}} \\[2ex] C_{f2} = \dfrac{1}{\omega_0 Z_5} = \dfrac{1}{\omega_0}\sqrt{\dfrac{P_L}{Z_{CM}V_2^2}} \\[2ex] L_1 = \dfrac{(Z_3 - Z_2)}{\omega_0} = \dfrac{1}{\omega_0}\sqrt{\dfrac{Z_{CM}V_1^2}{P_L}} \\[2ex] L_2 = \dfrac{Z_5}{\omega_0} = \dfrac{1}{\omega_0}\sqrt{\dfrac{Z_{CM}V_2^2}{P_L}}. \end{cases} \qquad (22)$$

It can be seen from (22) that the system with the proposed design method achieves power enhancement by solely modifying the source voltage and load voltage, without the
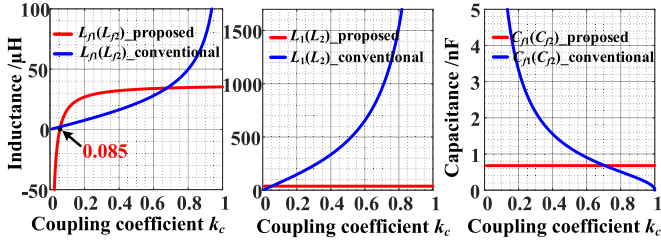
Fig. 7. Parameter comparison between the proposed and the conventional design method for the double-sided *LCL*-compensated topology with different coupling coefficients.

TABLE II
VOLTAGE STRESSES IN THE PROPOSED DESIGN METHOD

$$V_{Lf1} = -\frac{Z_{CM}Z_2}{Z_3 Z_5}V_2 \qquad V_{Cf1} = V_1 + \frac{Z_{CM}Z_2}{Z_3 Z_5}V_2 \qquad V_{L1} = V_1 + \frac{Z_{CM}}{Z_5}(\frac{Z_2}{Z_3}-1)V_2$$

$$V_{Lf2} = \frac{Z_{CM}Z_2 Z_6}{Z_1 Z_3 Z_5}V_1 \qquad V_{Cf2} = V_2 + \frac{Z_{CM}Z_2 Z_6}{Z_1 Z_3 Z_5}V_1 \qquad V_{L2} = \frac{Z_{CM}Z_2}{Z_1 Z_3}(1-\frac{Z_6}{Z_5})V_1 - V_2$$

need to change any other parameters. By simplifying (22), the resonance condition with the proposed design method can be derived as

$$\omega_0^2 = \frac{C_1}{(L_1 - L_{f1})C_{f1}^2} = \frac{C_2}{(L_2 - L_{f2})C_{f2}^2} = \frac{1}{L_1 C_{f1}} = \frac{1}{L_2 C_{f2}}. \tag{23}$$

Based on (14), (22), and (23), the load-independent CC current output is given by

$$I_{RL} = \frac{\omega_0 C_{f1} C_{f2} V_1}{C_M}. \tag{24}$$

The input impedance Z_{in} can be derived by the power balance and is expressed as

$$Z_{in} = \frac{V_1^2}{I_{RL}^2 R_L} = \frac{C_M^2}{\omega_0^2 C_{f1}^2 C_{f2}^2 R_L} \tag{25}$$

which indicates that a load-independent CC output and input ZPA are realized.

Fig. 7 gives the parameter comparison between the proposed and the conventional double-sided *LCL* compensation network design method [19], [21]. It can be observed that in the case of a high coupling coefficient, inductances $L_1(L_2)$ and $L_{f1}(L_{f2})$ with the proposed design method are smaller, while capacitances $C_{f1}(C_{f2})$ are slightly larger. It is worth noting that inductances $L_1(L_2)$ are extremely large with the conventional *LCL*-compensated network design method, which is not feasible in a practical system. Thus, the conventional double-sided *LCL*-compensated network design method is not suitable for the strongly coupled system. Besides, it should be noted that the compensation inductances $L_{f1}(L_{f2})$ is less than 0 on the condition that $k_c < 0.085$ in the proposed system. This is because in this case, Z_3 decreases and Z_2 and Z_1 are less than 0, which is contrary to the premise that all impedances are positive. Thus, the proposed design method is more suitable for the strongly-coupled CPT system.

C. Analysis of the Voltage Stresses and Current Stresses

The voltages across L_{f1}, L_{f2}, C_{f1}, C_{f2}, L_1, and L_2 are defined as V_{Lf1}, V_{Lf2}, V_{Cf1}, V_{Cf2}, V_{L1}, and V_{L2}, respectively. The voltage stresses in the double-sided *LCL*-compensated CPT system employing the proposed compensation network design method are listed in Table II. The currents flowing through L_{f1}, L_{f2}, C_{f1}, C_{f2}, L_1, L_2, C_1, and C_2 are defined as I_{Lf1}, I_{Lf2}, I_{Cf1}, I_{Cf2}, I_{L1}, I_{L2}, I_{C1}, and I_{C2}, respectively, and can be obtained by dividing the voltage stress across the

compensation circuit components by the impedance. The voltage and current stresses in the double-sided *LCL*-compensated system employing the conventional compensation network design method can be obtained from [21] in which the voltage stresses of all resonated components have been listed. Fig. 8 illustrates the voltage stress comparison between the proposed and the conventional compensated topology design method. It can be observed that the voltage stresses of the *LCL*–*LCL* CPT system employing the conventional design method increase rapidly with the increase of k_c, but with the proposed design method, the voltage stresses gradually stabilize. Additionally, it should be noted that the voltages across L_{f1} and C_{f1} with the proposed design method are higher than those of the conventional design method at low coupling regions. The reason is as follows. The voltages across L_{f1} and C_{f1} employing the conventional design method are defined as V_{Lf1_con} and V_{Cf1_con}, respectively, which can be expressed as [21]

$$\begin{cases} V_{Lf1\_con} = \frac{C_M C_{f2} V_2}{(1-k_c^2)C_1 C_2} = \frac{k_c^2 C_{f2}}{C_M(1-k_c^2)}V_2 \\ V_{Cf1\_con} = V_1 + V_{Lf1\_con}. \end{cases} \tag{26}$$

According to Tables I and II, the voltage across L_{f1} and C_{f1} with the proposed design method can be calculated as

$$\begin{cases} V_{Lf1} = -\frac{Z_2}{k_c Z_5}V_2 = -\frac{k_c\sqrt{Z_{CM}P_L}-V_1}{V_2 k_c}V_2 \\ V_{Cf1} = V_1 + V_{Lf1}. \end{cases} \tag{27}$$

It can be observed from (26) and (27) that V_{Lf1_con} and V_{Cf1_con} are relevant to k_c^2, V_{Lf1}, and V_{Cf1} are relevant to k_c. Thus, at low coupling regions, V_{Lf1_con} and V_{Cf1_con} are larger than V_{Lf1} and V_{Cf1}, respectively. It should be noted that the plate voltage stresses are much lower with the proposed design method compared to the conventional design method, especially at regimes of high coupling coefficients.

Fig. 9 illustrates the current stress comparison between the proposed and the conventional compensated topology design methods. In systems employing conventional design methods, the currents flowing through the compensation capacitors are higher, especially under the circumstance of high coupling coefficients. Although the currents flowing through the compensation inductors with the proposed method increase with the coupling coefficient, the inductance with the proposed design method is much lower than those in the conventional design method, as shown in Fig. 7. Therefore, the efficiency with the proposed design method is higher in areas of high coupling. Based on the above analysis, the proposed design
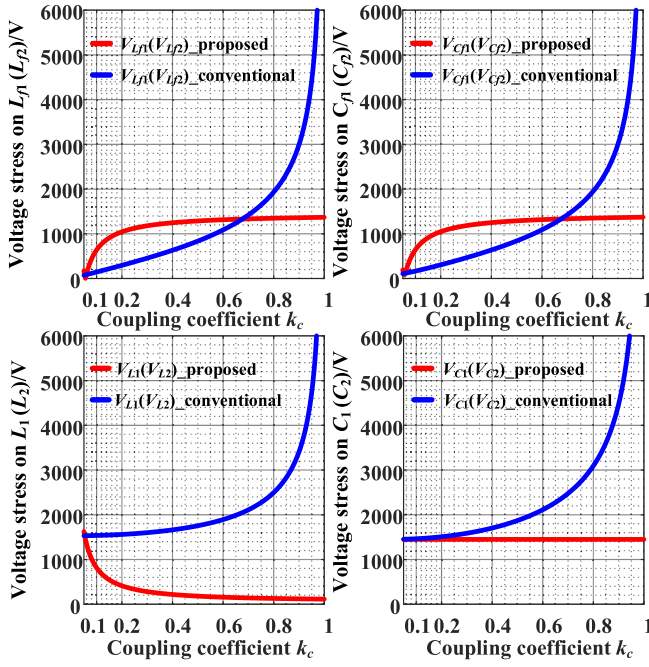
Fig. 8. Voltage stress comparison between the proposed design method and the conventional design method for the double-sided *LCL*-compensated CPT system.
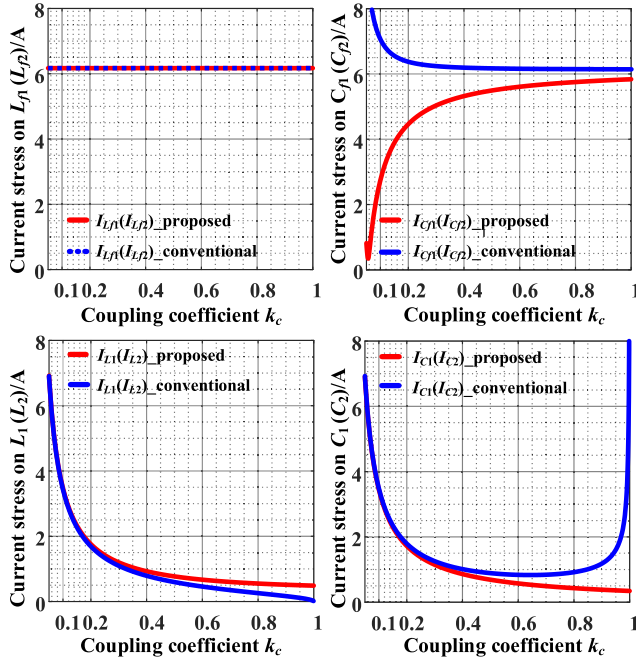

Fig. 9. Current stress comparison between the proposed and the conventional design method for the double-sided *LCL*-compensated CPT system.

methodology is better suited to an application with a high coupling coefficient.

D. Analysis of the System Efficiency

The system efficiency can be determined using the methodology outlined in [31], which involves listing the node voltage equations for the equivalent circuit to calculate the currents flowing through the compensation circuit components and
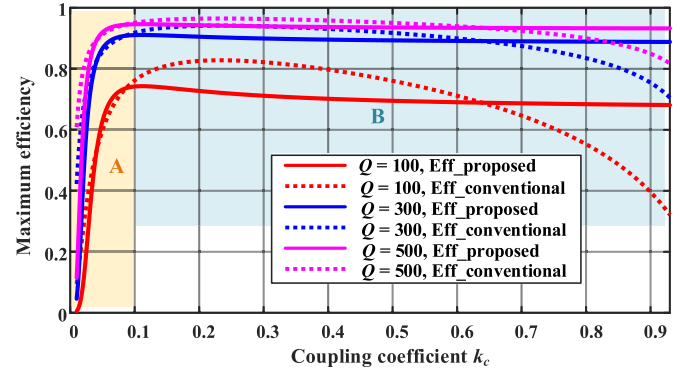

Fig. 10. Maximum achievable efficiency comparison between the proposed design method and the conventional design method versus different coupling coefficients with different quality factors.

obtaining efficiency by the ratio of output power to input power. The result reveals that the system efficiency is correlated with both the coupling coefficient and the quality factor. Usually, the quality factors of all compensation components are different. To simplify the efficiency analysis, all quality factors are assumed identical as Q. Fig. 10 shows the maximum efficiency comparison between the proposed and the conventional design method versus different coupling coefficients with different quality factors. It can be seen that a higher maximum system efficiency can be obtained with a higher quality factor with both the proposed and conventional design methods. The maximum achievable efficiency declines faster employing the conventional design method under the premise of a high coupling coefficient compared with that in the proposed design method. Besides, with a high coupling coefficient, the inductance L_1 (L_2) in the double-sided *LCL*-compensated CPT system employing the conventional design method obtained from [19] and [21] will reach the mH level, which is extremely large and not feasible in a practical system. Thus, the operation region of the double-sided *LCL*-compensated CPT system with the conventional design method is usually in range A, while the double-sided *LCL*-compensated CPT system with the proposed design method works in region B, which manifests that the proposed design method can have a higher efficiency. This characteristic also indicates that the proposed design method is beneficial to be applied to the high coupling coefficient scenario.

IV. SYSTEM VERIFICATION

A. Experiment Prototype

A 500 W experiment prototype has been developed as shown in Fig. 11. An inverter consisting of four SiC MOS-FETs (C2M0080120D) is used to generate the high-frequency ac power. The dc voltage of the inverter V_{dc} is 90V. The digital controller (TMS320F28335) is employed to generate pulsewidth modulation signals and the switching frequency is 1 MHz. On the secondary side, a rectifier consisting of four SiC diodes transforms the ac to dc. The coupler is constituted by four aluminum plates with the dimensions of 610 × 610 × 2 mm. The plate separation distance is 300 mm. The air-gap is 50 mm. In this case, the measured mutual capacitance C_M is

TABLE III
SYSTEM SPECIFICATIONS

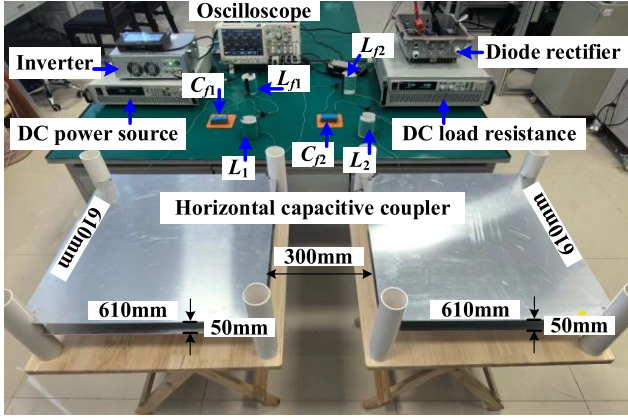| Parameter	Value	Parameter	Value
V_{dc}	90V	f	1MHz
Plate size	610mm×610mm×2mm	Separation distance	300mm
Air gap	50mm	k_c	0.82
C_M	37.86pF	$C_1(C_2)$	46.34pF
L_{f1}	34.82μH	L_{f2}	34.32μH
C_{f1}	677.68pF	C_{f2}	677.68 pF
L_1	37.38μH	L_2	37.38μH

Fig. 11. Experiment prototype.

about 37.86 pF, the measured self-capacitances C_1 and C_2 are about 46.34 pF, and the coupling coefficient k_c is about 0.82. The compensation inductors are made by 1200-strand Litz wires on a hollow plastic tube so that the conduction losses caused by the skin effect can be reduced. The compensation capacitors are formed by connecting multiple high-frequency film capacitors from KEMET in series and parallel to increase the withstand voltage and reduce the internal resistance. The system parameters are listed in Table III, which are obtained by using the process shown in Section III. It should be noted that the premise of obtaining the parameters is to ensure that the phase angle difference between V_{C1} and V_{C2} is 90°, and $V_{C1} = V_{C2}$ with a CC output and input ZPA. In practical applications, the strict input ZPA will increase the switching noises of the inverter, which induces system efficiency decrease and electro-magnetic interference increase, especially for high-frequency applications [32]. The way to solve it is to make the input current I_{Lf1} lag inverter output voltage V_{in} to facilitate zero-voltage switching (ZVS) [33]. According to (7), the output current I_{RL} is related to Z_{CM}, Z_1, Z_2, Z_3, Z_5, and V_1. In order not to affect the CC output characteristic, Z_6 can be adjusted to achieve ZVS. Thus, L_{f2} is slightly smaller than L_{f1} for the system to achieve ZVS.

B. Experiment Results

Fig. 12 illustrates experimental waveforms for load current I_o, inverter output voltage V_{ab}, inverter output current I_{Lf1}, rectifier input voltage V_{cd}, and rectifier input current I_{Lf2} under conditions of half load, 75% load, and full load conditions. The load currents are around 5.27, 5.16, and

TABLE IV
MEASURED LOAD CURRENTS AND SYSTEM EFFICIENCY

Normalized load resistance	0.5	0.75	1
DC load current	5.27A	5.16A	5.06A
Efficiency	86%	89%	90%

TABLE V
MEASURED LOAD CURRENTS AND SYSTEM EFFICIENCY

V_{dc}	Normalized load resistance	0.25	0.4	0.5	0.6	0.75	1
90V	DC load current	5.32A	5.30A	5.27A	5.25A	5.16A	5.06A
	Load power	125	200	250	300	375	500
	Efficiency	81.5%	84.5%	86%	88%	89%	90%
85V	DC load current	5.08A	5.04A	4.98A	4.95A	4.88A	4.84A
	Load power	111	178	223	268	334	446
	Efficiency	82%	86%	88%	89.5%	90.5%	90.2%
80V	DC load current	4.78A	4.74A	4.69A	4.65A	4.59A	4.56A
	Load power	99	158	198	237	296	395
	Efficiency	84%	88%	89.5%	90.3%	89.9%	90.1%
75V	DC load current	4.46A	4.45A	4.39A	4.36A	4.30A	4.25A
	Load power	87	139	173	208	260	347
	Efficiency	86%	89%	90.7%	90.5%	90.3%	90.1%

5.06 A, respectively. It shows that load output currents are nearly constant with different loads, which verifies that a CC output is achieved. The slight change in output current is caused by the parasitic resistances of the inductors and couplers. The corresponding system efficiency reaches 86%, 89%, and 90%, respectively. Table IV lists the experimental data. The inverter output voltages and currents are nearly in phase, which shows that the system has achieved the ZVS of MOSFETs. It is worth noting that the increase in the impedance angle with the decrease in load resistance is due to L_{f2} being slightly less than L_{f1} to achieve ZVS. Furthermore, the greater L_{f2} is reduced to achieve ZVS, the greater the variation in input impedance angle.

Fig. 13 shows the output load currents against the normalized load resistance with different input voltages. The current fluctuation ratio β is adopted to evaluate the CC output characteristic and is defined by

$$\beta = (I_{\max} - I_{\min})/I_{\max}. \tag{28}$$

It can be readily observed that β consistently remains below 5% amidst the normalized load resistance within 0.25–1, substantiating the robustness of the CC output. Furthermore, the power and efficiency performance across varied load scenarios with the input dc voltage within 75–90 V as illustrated in Fig. 14. It is worth noting that the system efficiency reaches 90% when the output load power is 500 W with an input voltage of 90 V when the normalized load resistance is 1. The maximum dc–dc efficiency reaching 90.7% is attained under a 75 V dc input voltage and an output power of 173 W. Table V lists the measured output currents and efficiency with different load resistances and power levels.

Fig. 15 illustrates the maximum system efficiency variation with an increasing coupling coefficient. The coupling coefficient can be adjusted by adding different external capacitors parallel to the capacitive coupler. In this case, only the
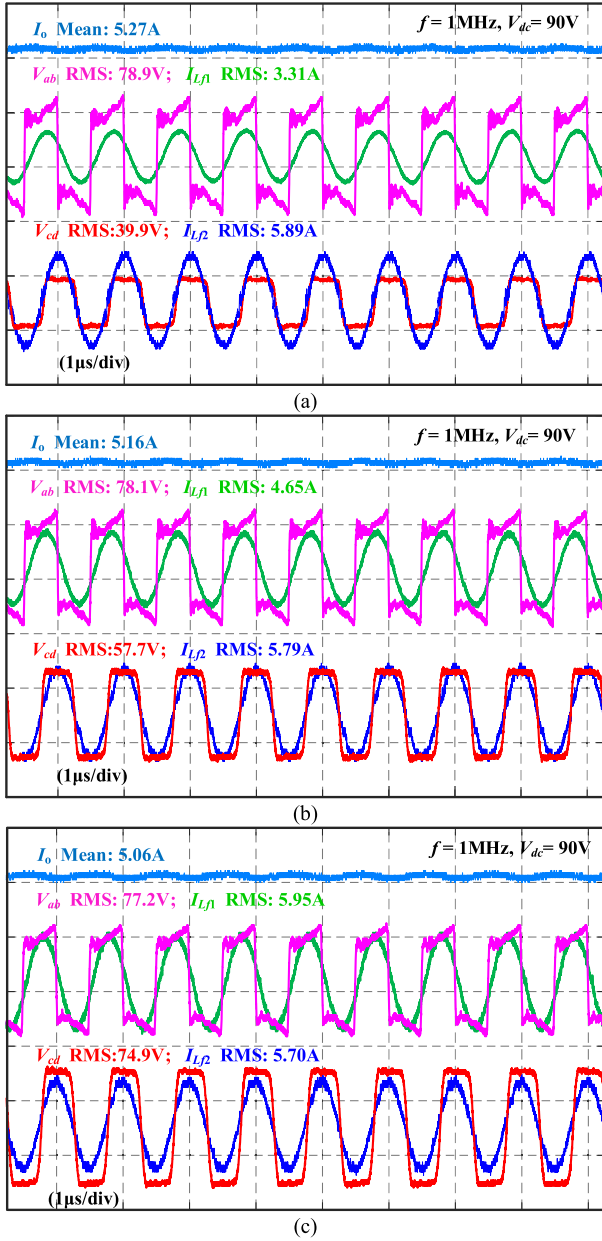
Fig. 12. Experiment waveforms with different load resistance at $k_c = 0.82$. (a) Half load. (b) 75% load. (c) Full load.
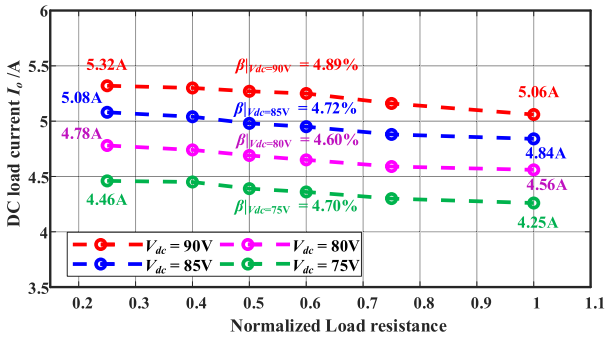

Fig. 13. Experiment results of output load current I_o against load resistance with different dc sources.

compensation inductances L_{f1} and L_{f2} will change, while all other parameters remain constant. The smaller the coupling coefficient, the smaller the compensation inductances L_{f1} and
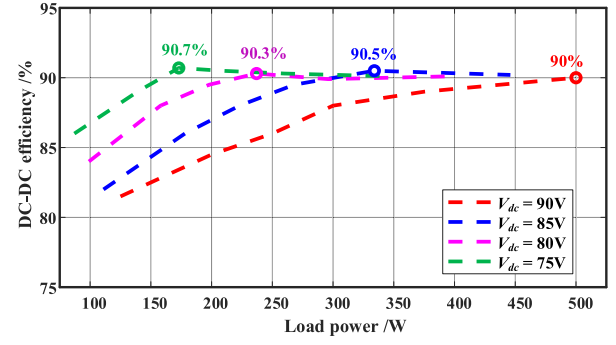

Fig. 14. Experiment results of system efficiency against load power with different dc sources.

TABLE VI
MEASURED SYSTEM EFFCIENCY

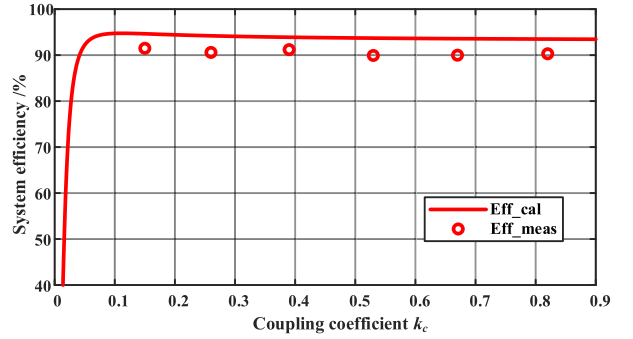| Coupling coefficient	0.15	0.26	0.39	0.53	0.67	0.82
System efficiency	91.5%	90.6%	91.2%	89.9%	90%	90.3%

Fig. 15. Experiment results of system efficiency against coupling coefficient.

L_{f2} become. The red curve is the calculated ac–ac efficiency, while the red dots represent the measured complete dc–dc system efficiency, including losses from both the inverter and rectifier. At coupling coefficients of 0.15, 0.26, 0.39, 0.53, 0.67, and 0.82, the measured maximum system efficiencies achieved are 91.5%, 90.6%, 91.2%, 89.9%, 90%, and 90.3%, respectively. The experimental data are listed in Table VI. It can be observed that the efficiency of the proposed method does not significantly change with the coupling coefficient and is consistent with the calculated efficiency trend.

The power loss ratio of the proposed design method with $k_c = 0.82$, $V_{dc} = 90$ V, and $P_o = 500$ W is shown in Fig. 16. Only the conduction loss is considered in the inverter because of ZVS [21]. The drain–source on-state resistance of MOSFET and the diode forward voltage of the reverse diode can be obtained from the datasheet. The power loss of the compensation component is caused by the current flowing through its parasitic resistance. The currents flowing through the inverter and compensation components can be calculated by solving Kirchhoff's current equations, then the power losses of the inverter and the compensation components can be estimated. Subtracting the loss of the inverter and all compensation components from the total loss from the measured efficiency, the loss of the coupler can be acquired [21]. The coupler plates
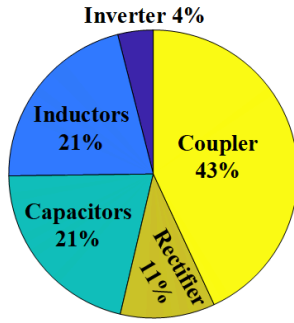
Fig. 16. Power loss ratio in the proposed design method when $k_c = 0.8$, $V_{dc} = 90$ V, and $P_o = 500$ W.

dissipate 43% of the power loss, which is significantly higher than other components.

Usually, the differential probe is used to measure the plate voltage. However, the proposed CPT system works at a high frequency (1 MHz), which is sensitive to parameter fluctuation. The differential probe contains an active circuit structure, and the intrinsic capacitance of the differential probe will have a large impact on the system because the intrinsic capacitances of differential probes are involved in resonance. In order to verify that the proposed voltage stresses are minimized, two external capacitors are added in parallel with the coupler and then the currents flowing through the external capacitors C_{ex1} and C_{ex2} are measured. When two small external capacitors are in parallel connected to the capacitive coupler with a coupling coefficient of 0.74, the currents flowing through the external capacitors are only 0.043 A, which is exceedingly small and challenging to measure accurately using current probes. Additionally, the current flowing through the external capacitor is directly proportional to the external capacitance. Consequently, in order to address this issue, two larger external capacitors, each with a capacitance of 100 pF, are connected in parallel with the coupler, thereby reducing the coupling coefficient k_c to 0.26. Since the mutual capacitance C_M is not changed, the compensation inductances L_1 and L_2 are the same as that in Table III and only the compensation inductance L_{f1} and L_{f2} are reduced to 29.31 μH. Fig. 17 illustrates experimental waveforms for the load current I_o, inverter output voltage V_{ab}, inverter output current I_{Lf1}, rectifier input voltage V_{cd}, and the currents flowing through external capacitors I_{Cex1} and I_{Cex2} under conditions of half load, 75% load, and full load conditions. The output load currents with the above three different load resistances are nearly constant, which shows that CC outputs are achieved. The phase angle difference between the primary-side plate voltage and the secondary-side plate voltage is around 90°, which indicates no reactive power is transferred and the plate voltages are minimized. The measured currents flowing through the external capacitors are shown in Table VII. The currents flowing through the secondary-side external capacitor I_{Cex2} are nearly constant because the voltage V_{C2} is independent of the load resistance. The currents flowing through the primary-side externally connected capacitor I_{Cex1} exhibit a direct proportionality to load resistance variation, and the currents flowing through the two externally connected capacitors are nearly equal at full load,

TABLE VII
MEASURED CURRENTS OF EXTERNAL CAPACITORS

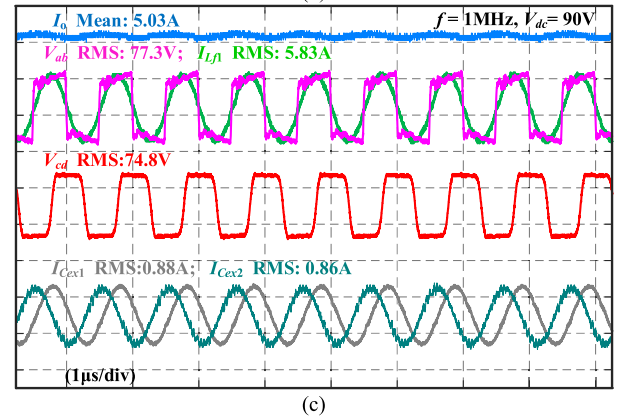| Normalized load resistance	0.5	0.75	1
I_{Cex1}	0.49A	0.69A	0.88A
I_{Cex2}	0.89A	0.88A	0.86A

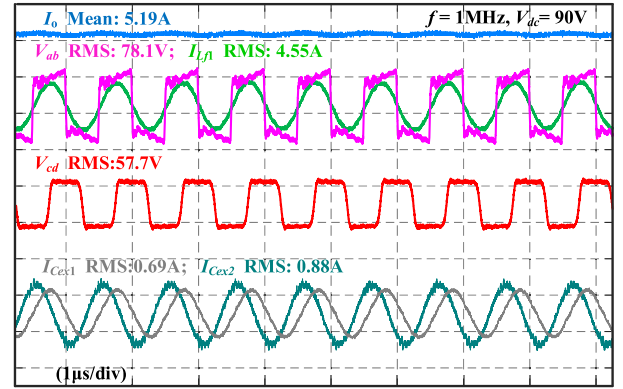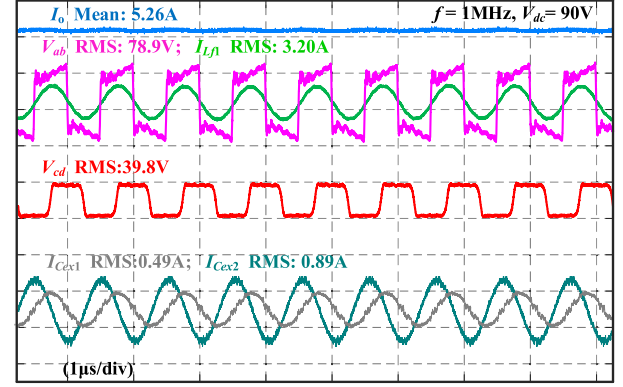Fig. 17. Experiment waveforms with different load resistance at $k_c = 0.26$. (a) Half load. (b) 75% load. (c) Full load.

with minor variations attributed to parasitic resistances within the system.

C. Comparison With Existing Works

Recently, voltage stress optimization has been considered a viable approach to mitigate the risks of air breakdown and electromagnetic interference in CPT systems. Lian et al.

TABLE VIII
CALCULATED PARAMETERS WITH DIFFERENT DESIGN METHODS

Parameter	[19, 21]	ω_1 in [26]	ω_{1H} in [26]	Proposed method
C_{ex1}	0pF	505.06pF	582.98pF	0pF
C_{ex2}	0pF	505.06pF	585.15pF	0pF
C_{f1}	478.27pF	9.8076nF	96.944pF	677.68pF
C_{f2}	478.27pF	9.8415nF	97.277pF	677.68pF
L_1	1696.9μH	48.738μH	582.46μH	37.78μH
L_2	1696.9μH	48.730μH	580.46μH	37.78μH
L_{f1}	52.96μH	2.5827μH	504.47μH	34.82μH
L_{f2}	52.96μH	2.5738μH	502.74μH	34.82μH

TABLE IX
VOLTAGE STRESS CONPARISION

| Parameter	[19, 21]	ω_1 in [26]	ω_{1H} in [26]	Proposed method
V_{C1} V_{C2} (RMS)	3250V	1457V	1457V	1450
θ	11.46°	82°	82°	90°
Safe distance	674mm	432mm	432mm	427mm

Fig. 18. Simulation waveforms of voltage stresses across the coupler. (a) Conventional design method. (b) Optimized design method with ω_1 in [26]. (c) Optimized design method with ω_{1H} in [26]. (d) Proposed design method.

[26] has proposed a parameter design method for an *LCLC*-compensated CPT system, in which three frequencies have been found to realize input ZPA and load-independent CC output under the premise of predesigned voltage stresses. The first frequency ω_1 is consistent with the conventional design method in [19] and [21]. The other two frequencies are ω_{1H} and ω_{1L}, which can be expressed as

$$\omega_{1H} = \omega_1\sqrt{1+\alpha}, \quad \omega_{1L} = \omega_1\sqrt{1-\alpha} \quad (29)$$

where

$$\alpha = \frac{\sqrt{(1-k_c^2)^2(C_2/C_{f2})^2 + (C_2/C_{f2})(1-k_c^2) + k_c^2}}{1 + (1-k_c^2)(C_2/C_{f2})}.$$

Applying the design method in [26] with the experimental coupler dimensions, the operating frequency is chosen to be 1 MHz with the predesigned minimum plate voltages of 2060 V for ω_1 and ω_{1H}, and 2050 V for ω_{1L}. The calculated parameters with the optimized method in [26] are shown in Table VIII, along with a comparison to the parameters of the proposed method as well as the conventional method in [19] and [21]. It should be noted that there is no solution for ω_{1L}. The compensation inductances are significantly reduced in the proposed method compared to the conventional method in [19] and [21]. Furthermore, unlike the optimization method in [26], no external compensation capacitors parallel to the capacitive coupler are needed, and there is a significant reduction in compensation inductances compared to the optimized parameters operating at ω_{1H}.

In the experimental setup, the parasitic capacitance of the probes affects circuit resonance, preventing direct measurement of the voltage stress across the plates. Therefore, voltage distribution on the plates is simulated and finite element simulations are employed to demonstrate electric field radiation. Without considering any parasitic resistances, the voltage stresses across the capacitive coupler in the double-sided *LCL*-compensated CPT system with the proposed and the conventional compensation network design method as well
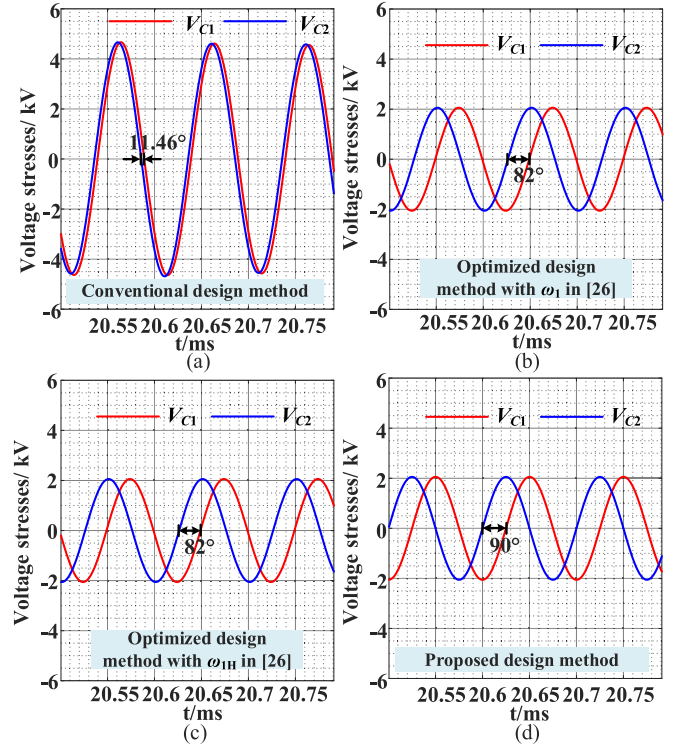
as the parameter design methods from [26] are simulated using LTspice, as shown in Fig. 18. Using the conventional design method, the rms values of the plate voltages are 3250 V, and the phase angle difference between the primary-side plate voltage and the secondary-side plate voltage is 11.46°, indicating that more reactive power is transferred. When the optimized design method in [26] is employed, the plate voltages at resonant frequencies ω_1 and ω_{1H} are both 1457 V with an increased phase angle difference of 82°, indicating that the plate voltages are not minimized, hence reactive power still exists. It is worth noting that the phase angle difference between the primary-side plate voltage and the secondary-side plate voltage is 90° with the proposed design method. This indicates no reactive power is transferred and the plate voltages are minimized, with rms values of 1450 V, significantly lower than the conventional design method. Based on the voltage stresses depicted in Fig. 18, the radiation of the leakage electric flux with the proposed and conventional design methods as well as the optimized method mentioned in [26] was investigated using Ansys/maxwell, and the results are presented in Fig. 19. In accordance with the IEEE standard [19], which sets the safety limit for electric fields at 1 MHz to be 614 V/m concerning human safety considerations, it is evident that the conventional design method requires a larger safe distance of 674 mm, the optimized design method in [26] requires a safe distance of 432 mm, while the safe distance determined by the proposed design method is 427 mm. The results mentioned above are listed in Table IX. This comparative analysis underscores the advantages of the
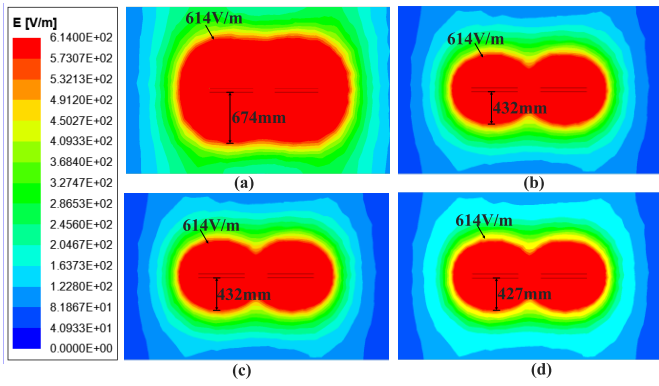
Fig. 19. Electric field distribution. (a) Conventional design method. (b) Optimized design method with ω_1 in [26]. (c) Optimized design method with ω_{1H} in [26]. (d) Proposed design method.

proposed design method, as it exhibits fewer compensation components, smaller compensation inductance, significantly lower voltage stresses, and reduced electric field emissions. These characteristics make it a highly promising choice for applications requiring high power levels.

V. Conclusion

This article proposes a double-sided *LCL* compensation network design method for the strongly coupled CPT system. Both ZPA and CC output characteristics can be obtained. No external capacitors are needed, and no reactive power is transferred from the primary side to the secondary side. Therefore, the voltage stress across the coupler plates is minimized. Compared with the conventional double-sided *LCL*-compensated network design method, the compensation inductances in the proposed design method are greatly reduced especially in the strongly coupled scenario, along with a substantial decrease in the radiation of the leakage electric flux. Experimental results have verified the proposed double-sided *LCL* compensation network design method and the experimental system can achieve 90% efficiency when 500 W power is delivered.

Acknowledgment

References

[1] B. Shi, F. Yang, C. Hu, and M. Ouyang, "Modelling and improvement of oscillation problem in a double-sided LCC compensation network for electric vehicle wireless power transfer," *eTransportation*, vol. 8, May 2021, Art. no. 100108.

[2] A. Ahmad, M. S. Alam, Y. Rafat, and S. Shariff, "Designing and demonstration of misalignment reduction for wireless charging of autonomous electric vehicle," *eTransportation*, vol. 4, May 2020, Art. no. 100052.

[3] S. Sinha, A. Kumar, B. Regensburger, and K. K. Afridi, "A new design approach to mitigating the effect of parasitics in capacitive wireless power transfer systems for electric vehicle charging," *IEEE Trans. Transport. Electrific.*, vol. 5, no. 4, pp. 1040–1059, Dec. 2019.

[4] S. Kodeeswaran, M. N. Gayathri, A. Kannabhiran, and S. S. Williamson, "Design of a static capacitive power transfer system with six-plate coupler for electric vehicle wireless charging," *IEEE Trans. Transport. Electrific.*, early access, Sep. 18, 2023, doi: 10.1109/TTE.2023.3316710.

[5] Y. Wang, H. Zhang, and F. Lu, "3.5-kW 94.2% DC–DC efficiency capacitive power transfer with zero reactive power circulating," *IEEE Trans. Power Electron.*, vol. 38, no. 2, pp. 1479–1484, Feb. 2023.

[6] J.-Q. Zhu, Y.-L. Ban, R.-M. Xu, and C. C. Mi, "An NFC-CPT-combined coupler with series- none compensation for metal-cover smartphone applications," *IEEE J. Emerg. Sel. Topics Power Electron.*, vol. 9, no. 3, pp. 3758–3769, Jun. 2021.

[7] X. Mou, D. Gladwin, J. Jiang, K. Li, and Z. Yang, "Near-field wireless power transfer technology for unmanned aerial vehicles: A systematical review," *IEEE J. Emerg. Sel. Topics Ind. Electron.*, vol. 4, no. 1, pp. 147–158, Jan. 2023.

[8] C. Park et al., "Separated circular capacitive coupler for reducing cross-coupling capacitance in drone wireless power transfer system," *IEEE Trans. Microw. Theory Techn.*, vol. 68, no. 9, pp. 3978–3985, Sep. 2020.

[9] C. Cai, X. Liu, S. Wu, X. Chen, W. Chai, and S. Yang, "A misalignment tolerance and lightweight wireless charging system via reconfigurable capacitive coupling for unmanned aerial vehicle applications," *IEEE Trans. Power Electron.*, vol. 38, no. 1, pp. 22–26, Jan. 2023.

[10] C. Jiang, B. Wei, C. Xu, X. Wu, and H. He, "Efficiency improvement under coupler misalignment for dual-transmitter and single-receiver capacitive power transfer system," *IEEE Trans. Power Electron.*, vol. 38, no. 12, pp. 14872–14883, Dec. 2023.

[11] M. Tamura, Y. Naka, K. Murai, and T. Nakata, "Design of a capacitive wireless power transfer system for operation in fresh water," *IEEE Trans. Microw. Theory Techn.*, vol. 66, no. 12, pp. 5873–5884, Dec. 2018.

[12] H. Zhang and F. Lu, "Insulated coupler structure design for the long-distance freshwater capacitive power transfer," *IEEE Trans. Ind. Informat.*, vol. 16, no. 8, pp. 5191–5201, Aug. 2020.

[13] J. Dai and D. C. Ludois, "A survey of wireless power transfer and a critical comparison of inductive and capacitive coupling for small gap applications," *IEEE Trans. Power Electron.*, vol. 30, no. 11, pp. 6017–6029, Nov. 2015.

[14] C. Cheng, Z. Zhou, W. Li, Z. Deng, and C. C. Mi, "A power relay system with multiple loads using asymmetrical coil design," *IEEE Trans. Ind. Electron.*, vol. 68, no. 2, pp. 1188–1196, Feb. 2021.

[15] Z. Cheng, Y. Lei, K. Song, and C. Zhu, "Design and loss analysis of loosely coupled transformer for an underwater high-power inductive power transfer system," *IEEE Trans. Magn.*, vol. 51, no. 7, pp. 1–10, Jul. 2015.

[16] F. Lu et al., "A high-efficiency and long-distance power-relay system with equal power distribution," *IEEE J. Emerg. Sel. Topics Power Electron.*, vol. 8, no. 2, pp. 1419–1427, Jun. 2020.

[17] F. Lu, H. Zhang, and C. Mi, "A review on the recent development of capacitive wireless power transfer technology," *Energies*, vol. 10, no. 11, p. 1752, Nov. 2017.

[18] Z. Zhang, H. Pang, A. Georgiadis, and C. Cecati, "Wireless power transfer—An overview," *IEEE Trans. Ind. Electron.*, vol. 66, no. 2, pp. 1044–1058, Feb. 2019.

[19] F. Lu, H. Zhang, H. Hofmann, and C. Mi, "A double-sided LCLC-compensated capacitive power transfer system for electric vehicle charging," *IEEE Trans. Power Electron.*, vol. 30, no. 11, pp. 6011–6014, Nov. 2015.

[20] F. Lu, H. Zhang, H. Hofmann, and C. C. Mi, "A double-sided LC-compensation circuit for loosely coupled capacitive power transfer," *IEEE Trans. Power Electron.*, vol. 33, no. 2, pp. 1633–1643, Feb. 2018.

[21] H. Zhang, F. Lu, H. Hofmann, W. Liu, and C. Mi, "A 4-plate compact capacitive coupler design and LCL-compensated topology for capacitive power transfer in electric vehicle charging applications," *IEEE Trans. Power Electron.*, vol. 31, no. 12, pp. 8541–8851, Jan. 2016.

[22] V.-B. Vu, M. Dahidah, V. Pickert, and V.-T. Phan, "An improved LCL-L compensation topology for capacitive power transfer in electric vehicle charging," *IEEE Access*, vol. 8, pp. 27757–27768, 2020.

[23] R. Mai, B. Luo, Y. Chen, and Z. He, "Double-sided CL compensation topology based component voltage stress optimisation method for capacitive power transfer charging system," *IET Power Electron.*, vol. 11, no. 7, pp. 1153–1160, Jun. 2018.

[24] H. Li, Y. Liu, and M. Fu, "Circular capacitive coupler with multilayer interleaving for stable output," *IEEE Trans. Microw. Theory Techn.*, vol. 71, no. 2, pp. 719–726, Feb. 2023.

[25] J. Lian and X. Qu, "Design of a double-sided LC compensated capacitive power transfer system with capacitor voltage stress optimization," *IEEE Trans. Circuits Syst. II, Exp. Briefs*, vol. 67, no. 4, pp. 715–719, Apr. 2020.
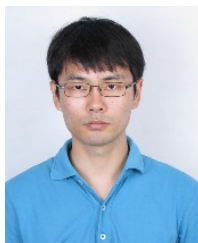
[26] J. Lian, X. Qu, X. Chen, and C. C. Mi, "Design of a double-sided LCLC-compensated capacitive power transfer system with predesigned coupler plate voltage stresses," *IEEE J. Emerg. Sel. Topics Power Electron.*, vol. 10, no. 1, pp. 128–137, Feb. 2022.

[27] Y. Su, S. Xie, A. P. Hu, C. Tang, W. Zhou, and L. Huang, "Capacitive power transfer system with a mixed-resonant topology for constant-current multiple-pickup applications," *IEEE Trans. Power Electron.*, vol. 32, no. 11, pp. 8778–8786, Nov. 2017.

[28] J. Lu, G. Zhu, D. Lin, Y. Zhang, H. Wang, and C. C. Mi, "Realizing constant current and constant voltage outputs and input zero phase angle of wireless power transfer systems with minimum component counts," *IEEE Trans. Intell. Transp. Syst.*, vol. 22, no. 1, pp. 600–610, Jan. 2021.

[29] R. He, P. Zhao, M. Fu, Y. Liu, H. Wang, and J. Liang, "Decomposition and synthesis of high-order compensated inductive power transfer systems for improved output controllability," *IEEE Trans. Microw. Theory Techn.*, vol. 67, no. 11, pp. 4514–4523, Nov. 2019.

[30] Y. H. Sohn, B. H. Choi, G.-H. Cho, and C. T. Rim, "Gyrator-based analysis of resonant circuits in inductive power transfer systems," *IEEE Trans. Power Electron.*, vol. 31, no. 10, pp. 6824–6843, Oct. 2016.

[31] T. Chen, C. Cheng, H. Cheng, C. Wang, and C. C. Mi, "A multi-load capacitive power relay system with load-independent constant current outputs," *IEEE Trans. Power Electron.*, vol. 37, no. 5, pp. 6144–6155, May 2022.

[32] Y. Jiang, L. Wang, J. Fang, C. Zhao, K. Wang, and Y. Wang, "A joint control with variable ZVS angles for dynamic efficiency optimization in wireless power transfer system," *IEEE Trans. Power Electron.*, vol. 35, no. 10, pp. 11064–11081, Oct. 2020.

[33] M. Wu et al., "A dual-sided control strategy based on mode switching for efficiency optimization in wireless power transfer system," *IEEE Trans. Power Electron.*, vol. 36, no. 8, pp. 8835–8848, Aug. 2021.

Xian Zhang received the M.E. and Ph.D. degrees in electrical engineering from Hebei University of Technology, Tianjin, China, in 2009 and 2012, respectively.

He is currently a Professor at Hebei University of Technology. He is the Director of China Electrotechnical Society and the Secretary-General of the National Specialized Committee on Wireless Power Transmission Technology. His research interests encompass intelligent high-power wireless power transmission technology, measurement of three-dimensional electromagnetic fields, and numerical calculations of modern engineering electromagnetic fields.

Guangyao Li received the B.S. degree in electrical engineering and intelligent control from Tianjin Sino-German University of Applied Sciences, Tianjin, China, in 2022. He is currently pursuing the M.E. degree in electrical engineering with Hebei University of Technology, Tianjin, China.

His research interests include engineering electromagnetism, wireless power transfer, and its industrial applications.

Yanjie Guo (Member, IEEE) received the Ph.D. degree in electrical engineering from the Institute of Electrical Engineering, Chinese Academy of Sciences, Beijing, China, in 2013.

He then joined the Key Laboratory of Power Electronics and Electric Drives, Chinese Academy of Sciences. He is currently an Associate Professor with the State Key Laboratory of Reliability and Intelligence of Electrical Equipment, Hebei University of Technology, Tianjin, China. His research interests include wireless power transfer, power electronics converters and control, energy systems and management, parameter identification, and state estimation.

Ting Chen (Member, IEEE) received the B.S., M.S., and Ph.D. degrees from China University of Mining and Technology, Beijing, China, in 2015, 2017, and 2022, respectively.

From November 2019 to November 2021, she was a joint Ph.D. Student with the Department of Electrical and Computer Engineering, San Diego State University, San Diego, CA, USA. She is now with the Department of Electrical Engineering and the State Key Laboratory of Reliability and Intelligence of Electrical Equipment, Hebei University of Technology, Tianjin, China. Her current research interests include wireless power transfer technologies, modeling, and control of switching converters.

Chunting Chris Mi (Fellow, IEEE) received the B.S.E.E. and M.S.E.E. degrees in electrical engineering from Northwestern Polytechnical University, Xi'an, China, in 1985 and 1988, respectively, and the Ph.D. degree in electrical engineering from the University of Toronto, Toronto, ON, Canada, in 2001.

He is a Distinguished Professor and the Chair of the Department of Electrical and Computer Engineering and the Director of the Department of Energy (DOE)-funded Graduate Automotive Technology Education (GATE), Center for Electric Drive Transportation, San Diego State University (SDSU), San Diego, CA, USA. Prior to joining SDSU, he was with the University of Michigan, Dearborn, MI, USA, from 2001 to 2015. His research interests include electric drives, power electronics, electric machines, electrical and hybrid vehicles, wireless power transfer, and power electronics.

Dr. Mi is a fellow of SAE. He was a recipient of the IEEE PELS Emerging Technology Award in 2019, the IEEE Transaction on Power Electronics Best Paper Award, two IEEE Transaction on Power Electronics Prize Letter Awards, and the Albert W. Johnson Lecture Award which is the highest distinction for any SDSU faculty.

Chenwen Cheng received the B.S. and Ph.D. degrees from Zhejiang University, Hangzhou, China, in 2012 and 2017, respectively, all in electrical engineering.

From 2018 to 2021, he was a Post-Doctoral Researcher at San Diego State University, San Diego, CA, USA. He is now with Southeast University, Nanjing, China. His research interests include motor control, renewable power generation, and wireless power transfer technologies.